HHS Public Access

Author manuscript

Phys Med Biol. Author manuscript; available in PMC 2016 July 07.

Published in final edited form as:

Phys Med Biol. 2015 July 7; 60(13): 5141–5161. doi:10.1088/0031-9155/60/13/5141.

Analytical Calculation of the Lower Bound on Timing Resolution for PET Scintillation Detectors Comprising High-Aspect-Ratio Crystal Elements

Joshua W. Cates[1], **Ruud Vinke**[1], and **Craig S. Levin**[1,2,3,4]

Craig S. Levin: cslevin@stanford.edu

[1]Department of Radiology, Stanford University, Stanford, CA, USA

[2]Department of Bioengineering, Stanford University, Stanford, CA, USA

[3]Department of Physics, Stanford University, Stanford, CA, USA

[4]Department of Electrical Engineering, Stanford University, Stanford, CA, USA

Abstract

Excellent timing resolution is required to enhance the signal-to-noise ratio (SNR) gain available from the incorporation of time-of-flight (ToF) information in image reconstruction for positron emission tomography (PET). As the detector's timing resolution improves, so does SNR, reconstructed image quality, and accuracy. This directly impacts the challenging detection and quantification tasks in the clinic. The recognition of these benefits has spurred efforts within the molecular imaging community to determine to what extent the timing resolution of scintillation detectors can be improved and develop near-term solutions for advancing ToF-PET. Presented in this work, is a method for calculating the Cramér-Rao lower bound (CRLB) on timing resolution for scintillation detectors with long crystal elements, where the influence of the variation in optical path length of scintillation light on achievable timing resolution is non-negligible. The presented formalism incorporates an accurate, analytical probability density function (PDF) of optical transit time within the crystal to obtain a purely mathematical expression of the CRLB with high-aspect-ratio (HAR) scintillation detectors. This approach enables the statistical limit on timing resolution performance to be analytically expressed for clinically-relevant PET scintillation detectors without requiring Monte Carlo simulation-generated photon transport time distributions. The analytically calculated optical transport PDF was compared with detailed light transport simulations, and excellent agreement was found between the two. The coincidence timing resolution (CTR) between two 3×3×20 mm^3 LYSO:Ce crystals coupled to analogue SiPMs was experimentally measured to be 162±1 ps FWHM, approaching the analytically calculated lower bound within 6.5%.

1. Introduction

Precise measurement of the difference in arrival times of annihilation photons at the detector ring of a PET system facilitates event localization along the line-of-response (LOR) between two detection elements. Incorporating this information into the image reconstruction process produces a gain in image SNR, relative to the case where no timing information is available, where events along a LOR are distributed evenly during line projection operations. The

magnitude of the SNR gain in reconstructed images increases as the system's timing resolution improves and can be estimated with Eq. (1), where *D* represents diameter of the volume of interest, *c* is the speed of light, and *CTR* is the coincidence resolving time of the system [Conti et al. 2008].

$$SNR_{Gain} = \frac{SNR_{ToF}}{SNR_{Non-ToF}} = \sqrt{\frac{D}{c \times \frac{CTR}{2}}} \quad (1)$$

Commercial whole-body PET systems with ToF capabilities currently achieve a CTR of approximately 500 ps FWHM [Jakoby et al. 2011, Bettinardi et al. 2011, Surti et al. 2007], providing an event localization of about 7.5 cm. Improving system CTR below 200 ps FWHM would produce an image SNR gain greater than a factor of three and event localization of about 3 cm, relative to the case where no ToF information is used. As system CTR improves to 100 ps these values improve to a factor of five and 1.5 cm, respectively. Therefore, timing improvements of these magnitudes facilitate substantial improvements in image SNR that translate to enhanced detection sensitivity and quantification of disease signatures. Additional benefits of improved CTR are reducing scanning time or injected tracer activity by an amount proportional to the SNR gain, thereby increasing patient throughput or reducing patient radiation dose.

Measured CTRs approaching or below 100 ps FWHM have been reported for $LaBr_3$:Ce and LSO:Ce,Ca(0.4%) crystals ≤5 mm in length and small cross-section ~3×3 mm^2 [Schaart et al. 2010, Wiener et al. 2010, Gundacker et al. 2013a]. However, crystal lengths of 20 mm or greater are necessary for an appropriate level of sensitivity for detecting annihilation photons in whole-body PET. In clinical PET systems, a PET detector comprises arrays of high-aspect-ratio (HAR) crystal elements, where the length is almost 7 times the width. For these crystals, variances in scintillation light photon propagation time to the photodetector as well as attenuation are more significant. This crystal geometry creates a large variation in the transit time of scintillation photons from their initial luminescence centers to the photosensor coupled to the exit interface of the crystal, degrading timing performance. At this point, a number of groups have also reported sub-200 ps FWHM CTR measurements with LYSO:Ce, LSO:Ce with various amounts of calcium co-doping, and $LaBr_3$:Ce of HAR crystals with 20 mm length or greater [Wiener et al. 2010, Yeom et al. 2013a, Gundacker et al. 2013b]. Additionally, measured CTRs of 3×3×20 mm^3 LYSO:Ce elements approaching 150 ps FWHM have been reported when coupled to a high quantum efficiency (QE) digital silicon photomultiplier [Yeom et al. 2014]. Simulation studies have also predicted that the timing resolution with HAR crystals could potentially approach 100 ps FWHM with increased photon statistics [Gundacker et al. 2013b], which could come from improved photosensor technology, light extraction techniques, new materials of higher light output and faster luminescence dynamics, and optimized readout electronics. In light of the progress the ToF-PET instrumentation community has shown on improving the timing resolution of HAR scintillation detectors, it is of particular interest to investigate what the minimum achievable timing resolution is for HAR scintillators with current measurement technologies.

A calculation of the lower bound on the timing resolution of scintillation detectors via the Cramér-Rao relationship was first outlined in [Seifert et al. 2012a]. The calculation showed good agreement with trends in literature, and improvements in timing resolution were explored with this method. One of the major assumptions in that work was that the spread in the propagation time of scintillation light was negligible when compared to the transit time spread of induced charge in a photosensor. Therefore, using that formalism, the calculated *CRLB* will be artificially lower than the real intrinsic limit, when compared with scintillators of HAR geometries. This work outlines a methodology for calculating the *CRLB* on the timing resolution of scintillation detectors with long crystal geometries, where the optical path length spread influences the achievable timing performance. An analytical PDF is presented to describe the optical transport of scintillation emissions. This PDF was validated against light transport simulations of HAR crystals. It is then demonstrated how the statistical limit on timing resolution can be calculated using this model and distributions describing the temporal profiles of a scintillator and photosensor.

1.1. Originality of this Approach

Two recent publications [Vinke et al. 2014, Gundacker et al. 2014] and an associated thesis [Gundacker 2014] have demonstrated how the *CRLB* on timing resolution can be calculated for scintillators with non-negligible photon transport using Monte-Carlo generated photon transit time distributions. In this work, we formulate the *CRLB* for HAR scintillators with a purely mathematical expression by using a closed-form solution for optical transit time spread. Such an approach has great utility, as it allows methods for achieving ultra-precise timing resolution with HAR scintillators with a simple mathematical expression, rather than relying on exhaustive Monte-Carlo studies. Researchers can easily adapt this methodology to their own applications. The final expression also represents an elegant form of the statistical limit on timing resolution for scintillation detectors with non-negligible photon transport.

2. Methods

The formulation of the optical transport PDF is shown according to the method outlined in [Yang 2012, Yang et al. 2013]. However, in that work, the analytical optical path length was given for crystals with no reflector and without regard to the extraction efficiency at the exit boundary. In this work, the PDF for optical path length is given for crystals wrapped in reflective materials and with attention to optics at the exit interface, i.e. the side of the crystal which is optically coupled to a photosensor. Section 2.1 focuses on an outline of the model with these alterations. The optical transport PDF is expressed specifically for a scintillation crystal element of rectangular parallelepiped geometry. In order to precisely match the derived model to experimental conditions Section 2.3, an air gap is assumed between the crystal and reflector material, and optical transport is considered for crystals with polished surfaces and specular reflectors. However, the light transport model can be easily adapted for cases where the reflector is optically coupled to the scintillator following the methodology outlined in [Yang et al. 2013] and altering the terms binding the expressions that comprise the analytical model. The accuracy of the light transport model in describing scintillators wrapped in diffuse reflectors is also assessed in Section 3.2. The

equations necessary for expressing the optical transport PDF and the calculation of the CRLB are presented for completeness, but detailed derivations of both can be found in [Yang et al. 2013] and [Seifert et al. 2012a, DeGroot 2012], respectively.

2.1. Analytical Expression for Light Transport

The probability of a forward traveling scintillation photon having a path length between x and $x+dx$ in a crystal of rectangular parallelepiped geometry with width w and length L, at a distance h from the bottom of the geometry can be expressed with Eq. (2).

$$f(x)_{for} = \begin{cases} 0, & x<h \\ h\frac{(\frac{x}{x-dx}-1)}{2x}(1-R_x), & h \le x \le \frac{h}{sin(\frac{\pi}{2}-\Theta_{c_x})} \end{cases} \quad (2)$$

R_x represents Fresnel's coefficient of reflectivity at the exit boundary where a crystal-grease interface exists. The lower bound of this expression is length h, which is the distance traveled directly from the position of interaction to the exit surface. The upper bound represents the path length of a photon that reflects by total-internal-reflection (TIR) off the side of the scintillator due to the crystal-air interface and impinges the exit boundary at the critical angle of the crystal-grease interface, Θ_{c_x}. The probability for a path length between x and $x + dx$ is given by projecting the conic area these path lengths form at the exit boundary onto a unit-sphere and comparing the surface area of this projection to the 4π emissions of scintillation light, as illustrated in figure 1. It is also noted that Eq. (2) is shown in a reduced form.

The probability of a scintillation photon to travel away from the photosensor with a total path length between x and $x + dx$ can be described with Eq. (3).

$$f(x)_b = \begin{cases} 0, & x<2L-h \\ (2L-h)\frac{\frac{x}{x-dx}-1}{2x}R_r, & 2L-h \le x \le \frac{2L-h}{cos(\Theta_{c_g})} \\ (2L-h)\frac{\frac{x}{x-dx}-1}{2x}(1-R_x), & \frac{2L-h}{cos(\Theta_{c_g})}<x \le \frac{2L-h}{sin(\frac{\pi}{2}-\Theta_{c_x})} \end{cases} \quad (3)$$

Eq. (3) equals zeros below a distance of $2L - h$, which is the shortest distance a back-reflected photon can have, traveling straight upward and then straight back downward to the exit boundary. Path lengths of back-reflected photons longer than this value represent those that impinge the top of the crystal at an angle less than the critical angle (Θ_{c_g}) for the scintillator-air interface until Θ_{c_g} is reached. In this region, the reflection coefficient, R_r, is determined by the wavelength and angular dependent properties of the reflector material. Once Θ_{c_g} is reached, transport to the exit boundary is again guided by TIR until the critical angle for the scintillator-grease interface at the exit is reached. Good illustrations of photon probability per path length in the direction opposite of the crystal's exit surface can be found in Figures 2.19 and 2.22 of [Yang 2012]. The expressions for forward and back-reflected photons overlap in regard to distance traveled for certain positions of interaction and crystal dimensions. Therefore, a complete expression for optical path length is given by Eq. (4).

$$f(x)=\frac{f_{for}(x)+f_b(x)}{\int_0^\infty (f_{for}(x)+f_b(x))dx} \quad (4)$$

Eq. (4) expresses the optical transit of scintillation light in terms of distance traveled, but this PDF can be transformed to represent the optical transit time of scintillation photons by considering that the transit time is simply the distance traveled divided by (*c*/*n*), where c is the speed of light in a vacuum and n is the index of refraction of the crystal. The optical transport PDF will be represented as a function of time, *f*(*t*), for the rest of this manuscript. Eq. (4) represents the optical transport of scintillation light for a particular position of interaction, but a measured CTR between two detectors is characterized by interactions at multiple positions along a scintillation crystal. The probability distribution of optical transit time over all positions of interaction can be expressed by

$$f(t)=\sum_{i=0}^{L} f(t_g+t)_i \times w_i \quad (5)$$

where w_i represents the weight for a particular position of interaction given from the attenuation of annihilation photons in the scintillation crystal, calculated according to $e^{\mu(L-h)}$, and t_g is the time-of-flight of an annihilation photon from the top of the crystal to a position of interaction.

With an analytical PDF for optical transport in place, the contribution to timing uncertainty made by the optical transit time spread was determined. The standard deviation of the propagation time of scintillation photons can be calculated by taking the square root of the difference in the first and second moments of the expectation value of the attenuation-weighted photon transit time PDF, Eq. (5), as shown in Eq. (6).

$$\sigma_{trans}^2=E[f(t)^2]-E[f(t)]^2$$
$$\sigma_{trans}=\sqrt{\int_{-\infty}^{\infty} t^2 \times f(t)dt-\left(\int_{-\infty}^{\infty} t \times f(t)dt\right)^2} \quad (6)$$

2.2. The Cramér-Rao Lower Bound on Timing Resolution

The temporal distribution of a scintillator's emissions, $p_{t_e}(t)$, can be expressed as a linear combination of bi-exponential models for any number of luminescence processes *i* that occur with probability $P_{ec,i}$. Here, $P_{ec,i}$ represents a number between 0 and 1 that properly weights each bi-exponential component.

$$p_{t_e}(t|\Theta)=\sum_i P_{ec,i}\frac{1}{(\tau_{d,i}-\tau_{r,i})}\left[e^{-\frac{t-\Theta}{\tau_{d,i}}}-e^{-\frac{t-\Theta}{\tau_{r,i}}}\right] \quad (7)$$

In Eq. (7), τ_r and τ_d are the rise and decay constants that characterize the emissions distribution, and Θ represents the interaction time of incident radiation in the scintillator.

Performing a convolution of Eq. (4), expressed as a function of time, with Eq. (7) will produce the distribution of arrival statistics at the exit boundary of the crystal, p_{trans}.

$$p_{t_{trans}}(t|\Theta)=\int_0^\infty p_{t_c}(t-\tilde{t}|\Theta)\times f(\tilde{t})d\tilde{t} \quad (8)$$

In order to calculate the lower bound on timing resolution, the variance in optical transport spread must be considered for all positions of interaction, as in Eq. (5). A convolution of Eq. (8) with a normal distribution having a width that corresponds to the charge transit spread in a photosensor will produce a distribution of primary triggers.

$$p_{t_{pt}}(t|D)=\int_0^\infty g(t-\tilde{t})\times p_{t_{trans}}(\tilde{t}_{trans})d\tilde{t} \quad (9)$$

Eq. (9) represents the distribution of primary triggers from the photosensor, in the absence of noise, under the condition D that the photons are detected.

The amount of information carried by a subset of N samples from a given PDF about a parameter Θ is described by the Fisher information. For this application, the expression for the Fisher statistic represents the amount of information on Θ carried by all available primary triggers and is written as

$$I_N(\Theta)=N\times\int_{-\infty}^{\infty}\left[\frac{\partial}{\partial\Theta}\ln p_{t_{pt}}(t|\Theta)\right]^2\frac{1}{p_{t_{pt}}(t|\Theta)}dt. \quad (10)$$

The Cramér-Rao relationship states that the variance of an unbiased estimator, Ξ_N, on Θ, the interaction time, is at least as large as the inverse of the Fisher information.

$$var(\Xi_N|\Theta)\geq\frac{1}{I_N(\Theta)} \quad (11)$$

Eq. (10) inherently assumes an ideal case where a timestamp is available from each detected photon and therefore forms the lower bound on the variance of the unbiased estimator on Θ. For comparison to achievable timing resolution in ToF-PET the *CRLB* is reported as the FWHM of a CTR between two identical detectors, according to Eq. (12), for the remainder of the manuscript.

$$CRLB=\frac{1}{\sqrt{I_N(\Theta)}}\times 2.35\times\sqrt{2} \quad (12)$$

2.3. Validation of Light Transport PDF with Simulation Models

To validate the optical transport PDF, the time of arrival of optical photons was simulated with the Monte Carlo component of optical transport code [ZEMAX 2014]. For these simulations, polished LYSO:Ce and ESR specular reflector were modeled with the optical

properties outlined in [Lőrincz et al. 2010]. One hundred thousand photons with a wavelength of 420 nm were generated isotropically at various depths along the center of crystal geometries. Two different scintillator geometries were simulated, and the propagation time of scintillation light from its origin to the exit of the crystal was compared with the time of arrival calculated by the optical transport PDF. Specifically, scintillation crystals of pixel geometries were simulated with 3×3×20 and 3×3×30 mm^3 dimensions. The two pixel geometries were chosen to assess the accuracy of $f(t)$ for modeling HAR crystal geometries.

Simulations were also performed with the reflector material having a Lambertian scatter profile for the 3×3×20 mm^3 geometry to assess the accuracy of the analytical model in predicting the photon transport time distribution for scintillators wrapped in diffuse reflectors, such as Teflon tape. Note that as the goal of this work is to optimize timing resolution, we have focused our studies on scintillators with polished surfaces; scintillators with their surfaces roughened are unanimously reported to have lower light collection [Lőrincz et al. 2010, Pawels et al. 2012, Heinrichs et al. 2002].

2.4. Experimental CTR vs. Calculated Statistical Limit

Coincidence timing resolution was measured between pairs of 3×3×5 mm^3 and 3×3×20 mm^3 LYSO:Ce crystals optically coupled to Hamamatsu S12572-50C silicon photomultipliers (SiPMs). The surfaces of the crystals were either wrapped in ESR reflector or Teflon tape in separate experiments, with an air gap left between the reflector and crystal surface. Teflon tape, a diffuse reflector, was used for the measurement with the 5 mm long crystals and one of two measurements with the 20 mm long crystals. An illustration of the experimental setup is shown in figure 2. The SiPM read-out electronics and experimental setup used were the same as described in [Yeom et al. 2013a]. The SiPMs were ac coupled to Minicircuits MAR-3+ preamplifiers, and their signals were split into timing and energy channels, then connected to an Agilent DSO940 2 GHz oscilloscope. Detector signals were sampled at 20 GSa/sec, and time-pickoff was performed off-line by leading edge discrimination on a full cubic spline of the timing signals. A baseline offset correction algorithm was used to compensate for shifts due to dark pulses [Vinke et al. 2009]. Coincidence events were selected within the full width at tenth maximum of a normal distribution fit to the 511 keV photopeak of each detector.

The calculated statistical limit on timing resolution was also compared with the measured CTR for the two LYSO:Ce detectors. The margin between the measured CTR for the 3×3×5 mm^3 crystals and the calculated *CRLB* for the measurement should be consistent with that observed between the CTR for 3×3×20 mm^3 crystals and the *CRLB* for that case, if optical photon transport is accurately incorporated into the calculation. Additionally, the CTR measurement with 3×3×20 mm^3 crystals wrapped in Teflon tape should match the value measured with ESR reflector for the assertion that this optical model can be applied to crystals wrapped with diffuse reflector to be validated.

The average light output of the LYSO:Ce crystals was previously measured using a single photon calibrated Hamamatsu R9779 PMT to be 9808±469 and 7684±722 photons/511 keV for the 5 mm and 20 mm long crystal, respectively. The average number of primary triggers

induced in the SiPMs from the interaction of annihilation photons in the crystals was found by integrating the PDE information on the SiPM's data sheet [Hamamatsu 2014], at the appropriate V_{ob}, over the emissions spectrum of LYSO:Ce. This effective PDE does not include the influence of dark counts and after pulsing. The single photon timing resolution (SPTR), 250 ps (FWHM), was also taken from the sensor's data sheet. The intrinsic rise and decay constants for the LYSO:Ce crystals were assumed to be 72±3 ps and 43±0.6 ns, respectively, as measured in [Seifert et al. 2012b].

3. Results

3.1. Optical Transport Spread in HAR Crystals

Figure 3(a) shows the calculated optical transport PDFs (Eq. (4)) for a 3×3×20 mm^3 crystal with the optical properties of LYSO:Ce and reflector properties of [Vikuiti 3M ESR 2014] for depths of interaction (DOI) at 2, 10, and 17 mm from the top of the crystal. The PDFs show a larger variance in the time of arrival of scintillation light at interaction locations close to the photosensor, with decreasing variance as the position of interaction occurs closer to the top of the crystal. This behavior is in agreement with the assertions and measurements presented in [Yeom et al. 2013a, Moses et al. 1999], and it is noted that the optical transport PDF matches simulation results for the same geometry and positions of interaction in [Yeom et al. 2013a]. Figure 3(b) shows the optical transport PDF when all positions of interaction are taken into account (Eq. (5)). This distribution is in agreement with a simulation of the arrival time of scintillation light from a simulation of a similar geometry in [Gundacker et al. 2013b] (2×2×20 mm^3 LSO:Ce,Ca(0.4%) was simulated in that work).

The calculated transit time spread (Eq. (6)) of scintillation photons in crystals with a 3×3 mm^2 cross-section and index of refraction of LYSO:Ce is shown for various lengths in figure 4. The transit time spread versus crystal length was found to trend according to a second-order polynomial.

In figure 5(a), two examples are given for p_{trans}, where $f(t)$ has been chosen for DOI at 1 mm and 19 mm from the top of a 3×3×20 mm^3 LYSO:Ce crystal. The inset of this figure shows the entire distributions, and the major portion of the figure shows the distributions at an early time window containing the statistics used for an estimate on time of interaction. An example of how the convolution of Eqs. (6)–(8) affects the time of arrival of photon statistics is displayed in figure 6(b). The PDF for LYSO:Ce's temporal emissions profile, $p_e(t)$, is shown in blue, and the optical transport distribution, $f(t)$, is shown for a 3×3×20 mm^3 crystal in green. The convolution of these two distributions, p_{trans}, is shown in red. When p_{trans} is convolved with a distribution representing charge transit spread, $g(t)$ in aqua, the resulting distribution for the temporal profile of the creation of primary triggers, p_{pt}, is shown in purple.

3.2. Validation with Simulation Models

Plots of the analytically calculated (Eq. (8)) and simulated time of arrival of scintillation photons for the 3×3×20 mm^3 crystal at DOI of 10 mm and 1 mm from the top of the crystal are displayed in figures 6(a) and (b), respectively. The same profiles are shown for 15 and 3

mm DOI for the 3×3×30 mm^3 geometry in figures 6(c) and (d). The optical transport PDF showed excellent agreement with the light transport simulations, validating $f(t)$ as an accurate analytical expression for the time of arrival of scintillation photons for crystals of these geometries.

Figure 7 shows examples of the comparison between the simulated and analytical photon arrival times for a 3×3×20 mm^3 LYSO:Ce pixel wrapped in a diffuse reflector. It can be seen that while the scatter from the diffuse reflector induces some blurring in photons having long path lengths in the crystal, the overall agreement is still quite good. For this crystal/reflector configuration, photons initially propagating towards the photosensor reach the critical angle of the exit interface before falling below the critical angle for the crystal/air boundary at the sides of the crystal. Therefore, few photons initially traveling in the forward 2π that reach the photosensor have interacted with the surrounding reflector. In fact, when considering the annihilation photon attenuation corrected optical photon arrival time for all positions of interaction (figure 7 (d)), there is very little difference in the analytical and simulated distributions. This suggests that, at least for polished crystals, the difference in the optical transport time variance for crystals with specular or diffuse reflectors might only have a very small effect on CTR. This assertion is tested in Section 3.3.

3.3. Calculated CRLB for HAR LYSO:Ce vs. Measured CTR

Figure 8 shows the measured CTR data between pairs of 3×3×5 mm^3 and 3×3×20 mm^3 LYSO:Ce crystals coupled to analogue SiPMs at the optimum LED threshold and bias V_{br}+4.6 V. The FWHM of the resulting distributions were 135±1 ps (5 mm length + Teflon), 162±1 ps (20 mm length + ESR), and 165±1 ps (20 mm length + Teflon). The error on these values was taken from the 95% confidence interval on the fit of the normal distribution to the data. The factor of ~6 reduction in dark counts with the S12572-50C SiPM, relative to the previous commercial version of this device (S1036233-050C) in combination with the baseline correction algorithms used in determining the LED threshold allowed the devices to be biased much higher than typically reported. This resulted in an integral PDE for LYSO:Ce of 41% [Hamamatsu 2014].

The measured CTR was compared with the calculated lower bound on timing resolution for these detectors as an experimental validation of the *CRLB* expression for HAR scintillation detectors. Figure 8 also shows the *CRLB* and the error associated with the calculation. The calculated lower bound on CTR for the 3×3×5 mm^3 crystals was 125±8ps, and 152±8 ps was calculated for the 3×3×20 mm^3 crystals. The error on these values was calculated in the manner outlined in [Seifert et al. 2012a]. The measured CTRs for the 3×3×20 mm^3 crystals approached the calculated statistical limit within 10 ps (within 6.5%) and 13 ps (within 8.6%) for the ESR and Teflon wrapped measurements, respectively. This margin is consistent with the 10 ps (8%) margin between the calculated *CRLB* and measured CTR with the Teflon wrapped 3×3×5 mm^3 crystals.

The measured CTR and the statistical limit on timing performance are not expected to overlap, as the experimental setup contains unavoidable processes such as noise. As mentioned in Section II. B, the *CRLB* assumes the availability of timing information from every detected photon. This is not the case with the analogue SiPMs used in this

experimental setup. Previous studies with short (≤5 mm in length) scintillation crystals have shown that the calculated *CRLB* without optical transport can be closely approach with analogue photosensors using digital pulse processing of signals and an optimized LED threshold [Seifert et al. 2012a, Cates et al. 2013, Post et al. 1950]. This same tendency was observed in figure 8 with HAR crystals.

The parameters in the *CRLB* calculation were varied to investigate the influence of various physical process on CTR with this experimental setup. Figure 9(a) shows the calculated statistical limit on CTR as a function of the normalized input parameters. For LYSO:Ce, improving the scintillation rise time has little influence on achievable timing resolution, as has also been reported in [Gundacker et al. 2013a, Seifert et al. 2012a]. With an experimentally measured rise time of 72±3 ps [Seifert et al. 2012b], this material has extremely fast early luminescence processes that do not dominate the contribution to timing uncertainty. The statistical limit on timing performance showed inverse relationships between the *CRLB* and the $\sqrt{N}$ and $\sqrt{\tau_d}$ dependence for photon statistics and decay time, respectively. This relationship is well known and has been previously reported in [Gundacker et al. 2013a, Fishburn et al. 2010, Hyman et al. 1964, Kronberger et al. 2010]. Calculated timing performance was found to improve linearly with SPTR. The calculation of the *CRLB* in figure 8 and figure 9(a) at normalized parameter value 1 uses the manufacturer's reported SPTR of 250 ps FWHM. Values reported for the SPTR of Hamamatsu MPPCs have varied from ~190–280 ps FWHM [Gundacker 2013c, Seifert 2012a]. However, these are reported for an older version of the photosensor used in this work, as noted in Section 3.3. Therefore, we have taken the manufactures value to be the most reasonable estimate SPTR for the SiPMs here. It is noted that large variations in SPTR of 20–30% lead to ~10–15 ps variations in the calculated *CRLB*. This can also be seen in figure 9(a).

Figure 9(b) shows the calculated *CRLB* on the CTR between two 3×3 mm^2 cross-sectional area LYSO:Ce crystals as the length was varied, holding all other parameters constant. This shows the influence of photon transport variance on achievable timing resolution. The *CRLB* showed a linear decrease below 20 mm until reaching 5 mm, where the influence of photosensor SPTR becomes dominant. It is noted that the value calculated at a crystal length of 5 mm precisely matches that calculated from Seifert's formalism of the *CRLB* [Seifert et al. 2012a], where no photon transport is incorporated, within <1%. The increase above 5 mm then represents the margin of error when using a formulation of the *CRLB* that does not account for optical photon transit and applying it to cases with non-negligible photon transit time variance. This figure also illustrates the utility of calculating the *CRLB* for HAR crystals with this approach. To compare with other efforts using a Monte-Carlo generated photon transit time distributions, a separate simulation would have to be run for each of these crystal lengths, totaling 38 separate simulations to perform this same investigation that was generated from simple calculations.

3.4. Achievable CTR with HAR LYSO:Ce Detectors

Figure 10 shows a colormap of the lower bound on CRT for 3×3×20 mm^3 LYSO:Ce scintillators, where available photon statistics and photosensor temporal response were

parametrically varied. A rise time of 72 ps and decay time of 43 ns, respectively were assumed for the calculation [Seifert et al. 2012b], and light output was considered to be 27,000 photons/MeV [Haas et al. 2008]. Note that the x-axis of this figure represents total detection efficiency, and it is comprised of both light collection efficiency at the exit interface of the crystal and the PDE of the photosensor used to convert scintillation light into charge. The light collection at the exit of crystal elements with polished surfaces and lengths of 20 mm is typically reported between 40–60% [Lőrincz et al. 2010, Bauer et al. 2009, Auffray et al. 2013, Pauwels et al. 2009, Levin et al. 2002]. The PDE of a photosensor tends to be between 20–30% for photomultipliers with bialkili photocathodes, and analogue SiPMs typically have an effective PDE of 30–35% when operated at a sufficient margin above the breakdown voltage, which is the case when the bias is optimized for timing measurements. Taking these factors into account, one arrives at a total optical photon detection efficiency in the range of 8–18%. The calculated *CRLB* in this region is consistent with the trend in literature of CTRs just above or below 200 ps when 20 mm length crystals are coupled to fast photosensors (SPTR ≤300 ps FWHM).

The lines in figure 10 labeled (1), (2), and (3) represent the *CRLB* for scenarios where advancements in crystal read-out or photosensor PDE were assumed. Scenario 1 represents the *CRLB* for the photon detection efficiency reported in Section 2.4. At a SPTR of 250 ps FWHM we have the calculated lower bound reported in figure 8(b). To approach a coincidence timing resolution of 100 ps FWHM, the timing performance of the photosensor must be significantly improved. For example, if the SPTR could be improved to values achievable with micro-channel plate photomultipliers (25–40 ps FWHM), the lower bound improves to ~110 ps. Scenario (2) represents the *CRLB* improvement for the case where light collection efficiency at the exit boundary is increased by 50%. This light collection increase represents a reported simulation value for increased light collection via photonic crystal techniques, for an LSO:Ce/grease exit interface [Lecoq et al. 2013]. At this level of light collection, the lower bound approaches 110 ps for SPTR values <200 ps. This improvement of the statistical limit on timing resolution for this scenario underscores the importance of ongoing research to improve the light extraction from inorganic scintillators. Scenario 3 shows the *CRLB* improvement when light collection is increased by 50% and photosensor PDE is improved to 50%. This PDE value is almost achievable with super-bialkali photocaothoes in PMTs [Nakamura et al. 2010], and the Philips DPC-3200 has a reported average effective PDE of nearly 40% at 420 nm [Philips Digital Photon Counting 2014]. Therefore, an assertion that photosensor technology could improve to have a PDE of 50% is not unrealistic. With these improvements, the calculated *CRLB* approaches 100 ps for SPTR values < 200 ps.

4. Discussion

The second order polynomial trend of the photon-transport-specific standard deviation in arrival time (Eq. (6) and figure 4) indicates that while the statistical spread in the transit time of photons increases with increasing crystal length, the effect diminishes for longer crystals. Referring to figure 3(b), this is attributed to the mean attenuation length of annihilation photons in the crystal length (12 mm for LYSO:Ce). The fact that most interactions occur near the top of the scintillation crystal minimizes the overall propagation time variation,

advantageously reducing the total variance for all interactions, relative to a uniform irradiation along the crystal's length. The photon transit time spread was also found to be comparable to the charge transit time spread of modern photosensors. This is an important finding, as it indicates improvements in the timing response of photosensor technology can still make an impact on achievable timing resolution with scintillation detectors comprising HAR crystal elements. The single photon timing resolution of photosensors must be much lower than 100 ps (σ) before the optical transport spread dominates the uncertainty contribution from transport processes. Here it is noted that the optical transport spread in figure 4 does not represent a limiting value on timing resolution. Since the combination of the scintillator's temporal emissions profile and the photon transit time dictate the distribution of photon statistics arriving at the photosensor, these two processes are not independent of each other. Therefore, a precise representation of achievable timing resolution should include a convolution of the scintillator's luminescence profile with transport processes in the crystal and photosensor to a global PDF (Eq. (9)). Referring to figure 5(b), these processes have a systemic effect on the distribution of primary triggers that comprise the detector's signal.

Figures 5(a) and 5(b) depict how the time of arrival of scintillation photons is altered by optical path length and how timing resolution is degraded by optical transit spread. The time of arrival of light created from an interaction near the photosensor has significant variance due to the difference in optical path lengths between forward traveling and back-reflected photons. Due to the greater transit time of back-reflected photons, they do not directly contribute to the earliest arriving scintillation photons, resulting in less statistics at the onset of a scintillation pulse, where an estimator of interaction time (ex. a leading edge trigger) is most optimum. In contrast, scintillation emissions from an interaction at the top of the crystal have little variance in optical transit time, resulting in the steeper rising edge for the distribution in figure 5(a). This results in an increase in early-arriving photon statistics, producing a more accurate estimation of time of interaction.

From data obtained in figure 8, the margin between the measured CTRs and statistical limit on these values was observed to be consistent between cases with minimal and significant optical photon transit time variance. This provides an additional experimental validation (in complement to the simulation studies in Sections 2.3 and 3.2) that the optical photon transit time variance is accurately accounted for in HAR crystal geometries using this formulation of the *CRLB*. Additionally, the assertion that this model can also be applied to polished crystals with diffuse reflectors was initially supported by the agreement between the modeled and simulated total optical photon transit time variance for this case (figure 7). Measured data in figure 8 also showed very small differences in the CTR for 3×3×20 mm^3 LYSO:Ce crystals (3 ps or 1.8% difference). Therefore, the calculated *CRLB* that includes the presented optical model also provides a good value for polished crystals wrapped in diffuse reflectors.

Figures 9 and 10 demonstrate that for scintillation detectors comprising HAR LYSO:Ce crystals, the uncertainty in timing performance is still dominated by photon statistics. Altering the number of detected photons in the calculation of the *CRLB* by a factor of 0.05–2 caused the statistical bound on CTR to fluctuate by as much as 600 ps. The same study with

photon statistics held constant while the crystal length was varied from 3–40 mm only affected the lower timing bound by ~20 ps. A major problem with scintillation crystals >20 mm in length is the significant light loss that occurs due to geometric factors, imperfections on the crystal surface (especially at corners [Gundacker et al. 2013a]), and absorption and scattering of light within the crystal element. However, a parametric investigation into the minimum achievable timing resolution with HAR LYSO:Ce detectors in Section IV. D revealed that with successful implementation of light extraction techniques and improvements in photosensor PDE toward 50%, timing performance approaching or below 100 ps is achievable with LYSO:Ce and single sided photosensor readout. An increase in photon statistics produces more primary triggers from forward traveling, early arriving scintillation light, regardless of the large transit time variance due to photons that initially propagate in the direction opposite of the photosensor. Therefore, despite the variance in photon transit time in HAR scintillation crystals, a calculation of the statistical limit on timing performance suggests that a CTR of 100 ps is still achievable with HAR LYSO:Ce scintillators, given progress on the maturity of light extraction techniques and innovations in photosensor technology.

Concerning the margin between the measured timing resolution and the predicted statistical limit, as in other reports, we have shown the lower bound can be closely approached using analogue photosensors. This is because the finite rise time of these devices causes an averaging of early arriving photons in the detector waveform, allowing them to intrinsically operate near the *CRLB* [Vinke et al. 2014]. However, it has been shown in [Seifert et al. 2012a, van Dam et al. 2013] that detectors with the ability to acquire multiple timestamps for a single interaction can provide information for maximum likelihood algorithms that allow them to operate at the statistical limit on timing resolution. Some of this margin is also attributed to processes unavoidable in experimental measurements such as noise. In a recent simulation study [Gundacker et al. 2014], it was demonstrated that the *CRLB* can be reached with a leading edge trigger on analogue SiPM signals that are free of noise.

In summary, the convolution of physical processes describing photon transit time, attenuation length of annihilation photons, charge transit time spread in the photosensor, and the number of photons incident on the detector that are converted to primary triggers dictates the achievable timing resolution with HAR scintillation detectors for ToF-PET. The most influential of these parameters being available photon statistics. Therefore, the most direct route to improved timing performance in ToF-PET is through novel light extraction techniques and improved photosensor PDE. However, improvements in detector SPTR are predicted to also drive CTR toward 100 ps FWHM for 3×3×20 mm^3 LYSO:Ce detectors (figures 7 and 8). It is simple enough to assert that improvements in light collection and detector SPTR will drive timing resolution to this level, but here we quantitatively identify improvements necessary toward ultra-precise timing performance with HAR scintillation detectors. The analytical formulation allows research avenues toward this performance to be accurately and easily identified, rather than performing multiple Monte Carlo simulation studies to provide the same information. The presented approach can be applied to any scintillation material, and it can be easily adapted to represent the *CRLB* for a variety of

approaches in improving timing performance (for example: Cherenkov radiators, dual sided readout of crystals, and monolithic crystal detectors).

5. Conclusions

A method for calculating the Cramér-Rao lower bound on timing resolution was developed for scintillation detectors comprising HAR crystal elements with right rectangular parallelepiped geometries using a closed-form solution for optical transport time. The analytical photon transport PDF was used to explore the effect optical path length spread has on the time of arrival of photon statistics at the exit boundary. With the optical transport PDF in place, the lower bound on timing resolution was calculated for HAR LYSO:Ce scintillation crystals with a purely mathematical expression. The calculated lower bound was compared with an experimentally measured CTRs between 3×3×5 and 3×3×20 mm^3 LYSO:Ce crystals coupled to analogue SiPMs. The two were found to correlate within 13 ps for all experimental configurations. The method outlined for calculating the *CRLB* was also used to investigate the limit of achievable timing resolution with HAR LYSO:Ce scintillators and detector instrumentation common to ToF-PET research. Further improvements towards 100 ps CTR were also identified by imagining improvements in light collection and photosensor response.

Acknowledgments

This work is supported by NIH grant R21 EB014405. This work is also partially supported by the Stanford Molecular Imaging Scholars (SMIS) Program (NIH-NCI grant R25 CA118681).

References

Auffray E, Frisch B, Geraci F, Ghezzi A, Gundacker S, Hillemanns H, Jarron P, Meyer T, Pagnoni M, Pauwels K, Pizzichemi M, Lecoq P. A comprehensive and systematic study of coincidence time resolution and light yield using scintillators of different size and wrapping. IEEE Trans Nucl Sci. 2013; 60:3163–71.

Bauer F, Corbeil J, Schmand M, Henseler D. Measurements and ray-tracing simulations of light spread in LSO crystals. IEEE Trans Nucl Sci. 2009; 56:2566–73.

Bettinardi V, Presotto L, Rapisarda E, Picchio M, Gianolli L, Gilardi MC. Physical performance of the new hybrid PETCT Discovery-690. Med Phys. 2011; 38:5394–411. [PubMed: 21992359]

Conti M. State of the art and challenges of time-of-flight PET. Phys Medi. 2008; 25:1–11.

DeGroot, MH. Probability and Statistics. Reading, MA: Addison-Wesley; 2012. p. 514-22.

Gundacker S, Auffray E, Frisch B, Jarron P, Knaptisch A, Meyer T, Pizzichemi M, Lecoq P. Time of flight positron emission tomography towards 100 ps resolution with L(Y)SO: an experimental and theoretical analysis. JINST. 2013a; 8:P07014.

Gundacker S, Knaptisch A, Auffray E, Jarron P, Meyer T, Lecoq P. Time resolution deterioration with increasing crystal length in a TOF-PET system. Nucl Instrum Methods A. 2013b; 737:92–100.

Gundacker S, Auffray E, Di Vara N, Frisch B, Hillemanns H, Jarron, Lang B, Meyer T, Mosquera-Vazquez S, Vauthey E, Lecoq P. SiPM time resolution: From single photon to saturation. Nucl Instrum Methods A. 2013c; 718:569–572.

Gundacker S, Auffray E, Jarron P, Meyer T, Lecoq P. On the comparison of analog and digital SiPM readout in terms of expected timing performance. Nucl Instrum Methods A. 2014 Available online 19 October 2014.

Gundacker, S. PhD thesis. Vienna University of Technology; 2014. Time resolution in scintillator based detectors for positron emission tomography.

Haas JTM, Dorenbos P. Advances in Yield Calibration of Scintillators. IEEE Trans Nucl Sci. 2008; 55:1086–92.

Hamamatsu. Hamamatsu S12572-025 MPPC Datasheet. 2014. http://www.hamamatsu.com

Jakoby BW, Bercier Y, Conti M, Casey ME, Bendriem B, Townsend DW. Physical and clinical performance of the mCT time-of-flight PET/CT scanner. Phys Med Biol. 2011; 56:2375–89. [PubMed: 21427485]

Lecoq P, Auffray E, an Knaptisch A. How Photonic Crystals Can Improve the Timing Resolution of Scintillators. IEEE Trans Nucl Sci. 2013; 60(3):1653–1657.

Levin CS. Design of a high-resolution and high-sensitivity scintillation crystal array for PET with nearly complete light collection. IEEE Trans Nucl Sci. 2002; 49:2236–43.

Lőrincz E, Erdie G, Péczeli I, Steinbach C, Ujhelyi F, Bükki T. Modeling and optimization of scintillator arrays for PET detectors. IEEE Trans Nucl Sci. 2010; 57:48–54.

Kronberger M, Auffray E, Lecoq P. Improving light extraction from heavy inorganic scintillators by photonic crystals. IEEE Trans Nucl Sci. 2010; 57:2475–82.

Nakamura K, Hamana Y, Ishigami Y, Matsui T. Latest bialkali photocathode with ultra high sensitivity. Nucl Instrum Methods A. 2010; 623:276–278.

Pauwels K, Auffray E, Gundacker S, Knaptisch A, Lecoq P. Effect of aspect ratio on the light output of scintillators. IEEE Trans Nucl Sci. 2009; 59:2340–45.

Philips Digital Photon Counting Leaflet. 2014. http://www.research.philips.com/initiatives/digitalphotoncounting/news/downloads/leaflet-digital-silicon-photomultiplier.pdf

Schaart DR, Seifert S, Vinke R, van Dam HT, Dendooven P, Lohner H, Beekman FJ. LaBr3:Ce and SiPMs for time-of-flight PET: achieving 100 ps coincidence resolving time. Phys Med Biol. 2010; 55:179–189.

Seifert, S.; Vinke, R.; van Dam, HT.; Lohner, H.; Dendooven, P.; Beekman, FJ.; Schaart, DR. ultra precise timing with SiPM-based TOF PET scintillation detectors. NSS/MIC: IEEE Nucl. Sci. Symp. Conf. Record; Orlando. 2009. p. 2329-33.

Seifert S, van Dam HT, Schaart DR. The lower bound on the timing resolution of scintillation detectors. Phys Med Biol. 2012a; 57:1797–1814. [PubMed: 22410975]

Seifert S, Steenbergen JHL, van Dam HT, Schaart DR. Accurate measurement of the rise and decay times of fast scintillators with solid state photon counters. JINST. 2012b; 7:P09004.

Surti S, Kuhn A, Werner ME, Perkins AE, Kolthammer J, Karp JS. Performance of Philips Gemini TF PET/CT scanner with special consideration for its time-of-flight imaging capabilities. Jour Nucl Med. 2007; 48:471–80. [PubMed: 17332626]

van Dam HT, Borghi G, Seifert S, Schaart DR. Sub-200 ps CRT in monolithic scintillator PET detectors using digital SiPM arrays and maximum likelihood interaction time estimation. Phys Med Biol. 2013; 58:3243. [PubMed: 23611889]

Vinke, R.; Seifert, S.; Schaart, DR.; Schreuder, FP.; de Boer, MR.; van Dam, HT.; Beekman, FJ.; Lohner, H.; Dendooven, P. Optimization of digital time pickoff methods for $LaBr_3$-SiPM TOF-PET detectors. NSS/MIC: IEEE Nucl. Sci. Symp. Conf. Record; Orlando. 2009. p. 2962-68.

Vinke R, Olcott PD, Cates JW, Levin CS. The lower timing resolution bound for scintillators with non-negligible optical photon transport in Time-of-Flight PET. Phys Med Biol. 2014; 59:6215–6229. [PubMed: 25255807]

Vikuiti 3M ESR Spectral Reflector. 2014. http://solutions.3M.com

Wiener, RI.; Kaul, M.; Surti, S.; Karp, JS. Signal analysis for improved timing resolution with scintillation detectors for TOF PET imaging. NSS/MIC: IEEE Nucl. Sci. Symp. Conf. Record; Knoxville. 2010. p. 1991-5.

Yang X, Downie E, Farrell T, Peng H. Study of light transport inside scintillation crystals for PET detectors. Phys Med Biol. 2013; 58:2144–2161.

Yang, X. Masters Thesis. McMaster Unviersity; 2012. Development of a monte carlo simulation tool for light transport inside scintillation crystals.

Yeom JY, Vinke R, Levin CS. Optimizing timing performance of silicon photomultiplier-based scintillation detectors. J Urol. 2013a; 133:230–235.

Yeom JY, Vinke R, Levin CS. Side readout of long scintillation crystal elements with digital SiPM for TOF-DOI PET. Medical Physics. 2014; 41:122501. [PubMed: 25471979]

ZEMAX. ZEMAX Development Crop. 2014. www.zemax.com

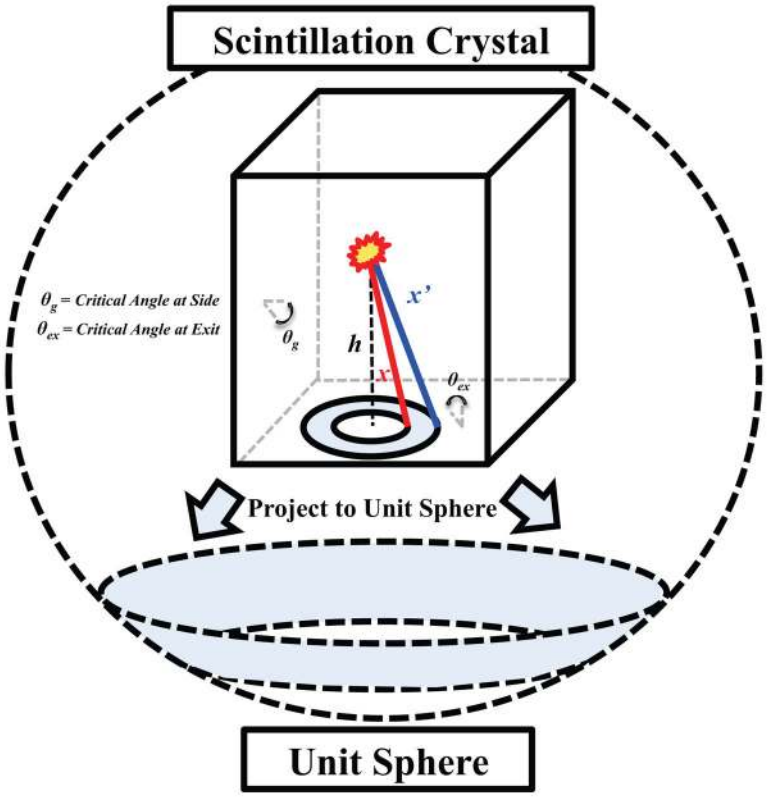

Figure 1.

Illustration of the methodology for deriving the analytical light transport time distribution. The probability of a photon having a path length between x and x+dx (x′) can be calculated by projecting the conic area created by the two paths onto a unit sphere.

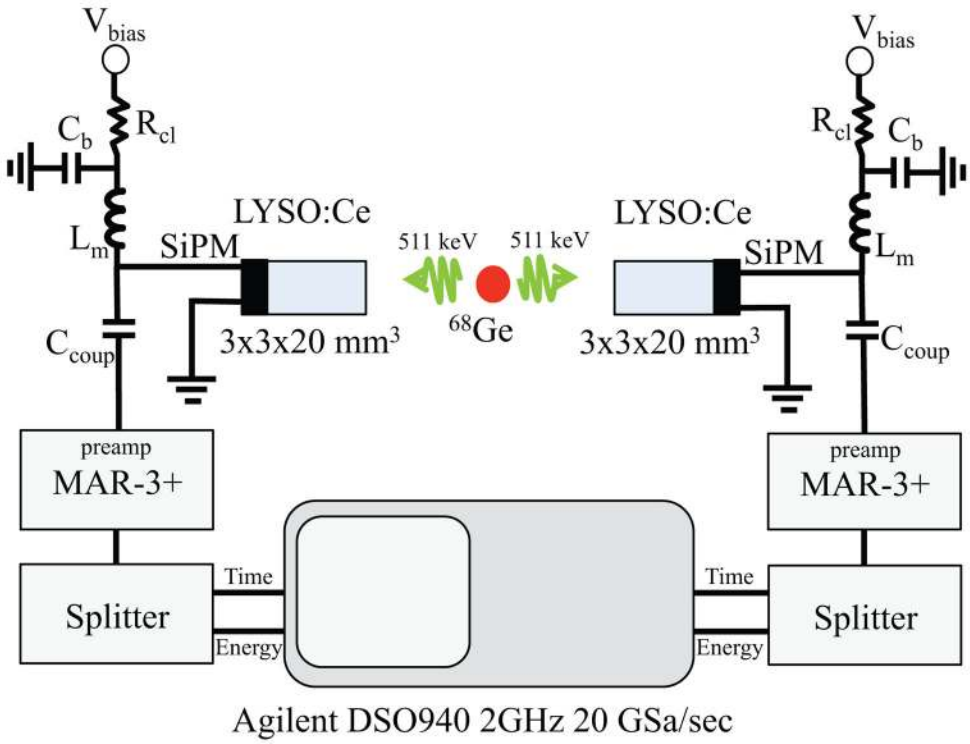

Figure 2.
Illustration of the experimental setup for the coincidence timing resolution measurement.

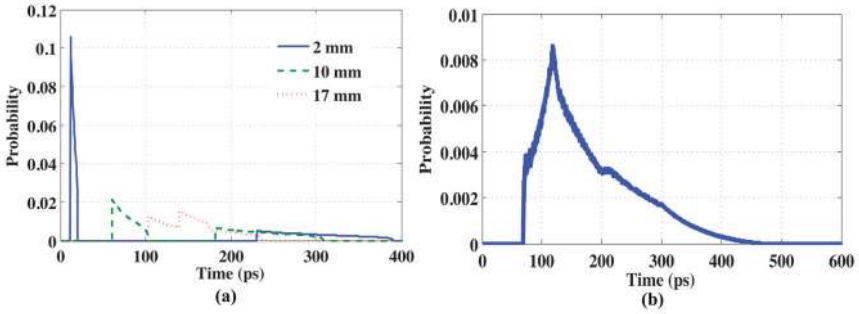

Figure 3.

The probability of the arrival time of photons produced at positions of interaction 2, 10, and 17 mm from the top of an 3×3×20 mm^3 LYSO:Ce crystal are shown in (a). In (b), the total probability of the arrival time over all possible interaction depths in the crystal is shown, where the probability of interaction and time of flight of annihilation photons before interaction are taken into consideration.

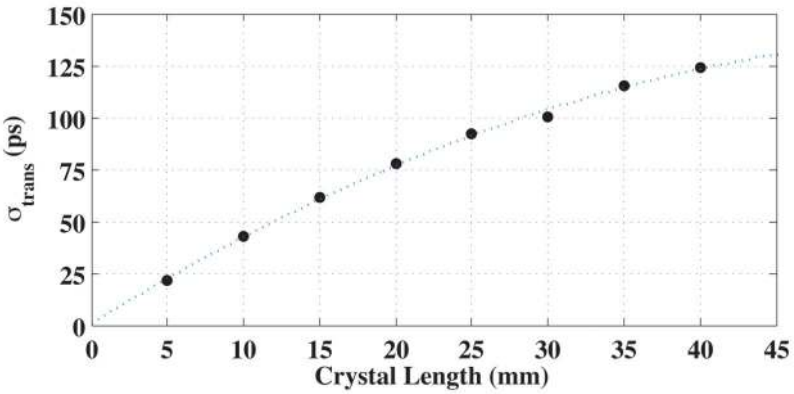

Figure 4.

The standard deviation in the photon transit time for crystals of 3×3 mm^2 cross-sectional area with index of LYSO:Ce is shown for different lengths.

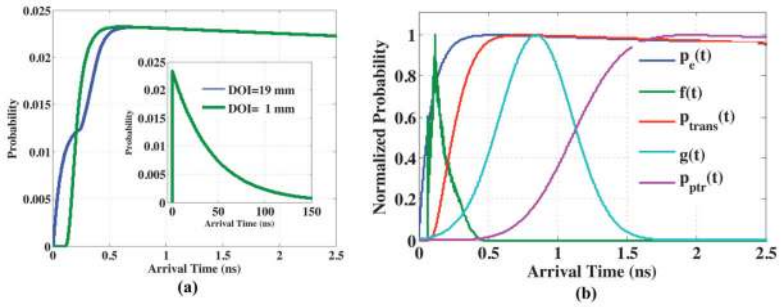

Figure 5.

The convolution of the optical transport PDF and the scintillator's temporal emissions profile for positions of interaction at 19 mm and 1 mm from the top of the crystal are shown in (a). In (b), the resulting PDFs from various convolutions are shown as $p_{t_{pt}}$ is calculated.

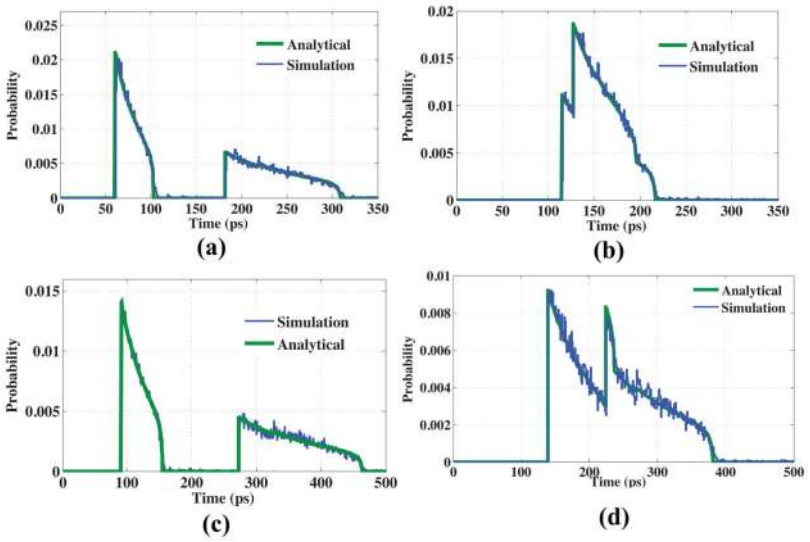

Figure 6.

Comparisons of the analytical optical transport PDF to light transport simulations for LYSO:Ce scintillators of various dimensions. In (a), the time of arrival of scintillation photons is shown for an interaction 10 mm from the top of a 3×3×20 mm^3 scintillator, and (b) shows the arrival times for an interaction at 1 mm from the top. The time of arrival of photons due to optical transit spread in a 3×3×30 mm^3 crystal for interactions 15 mm and 3 mm from the top are shown in (c) and (d).

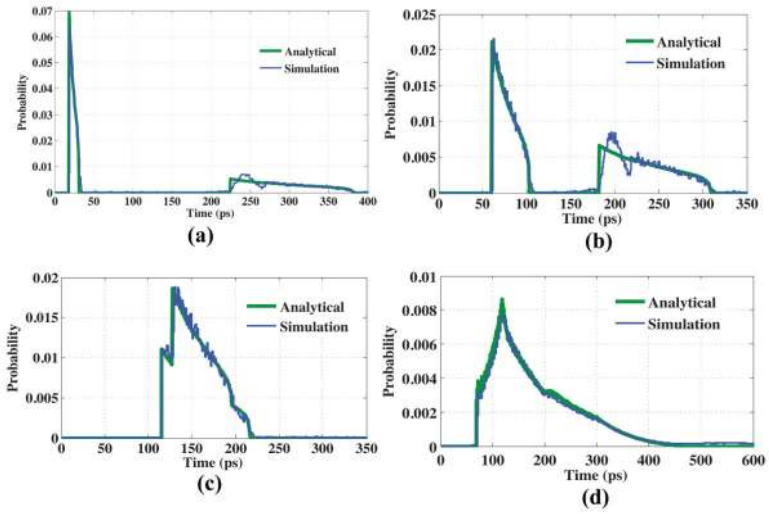

Figure 7.

The probability of the arrival time of photons produced at positions of interaction 17, 10, and 1 mm from the top of an 3×3×20 mm^3 LYSO:Ce crystal surrounded with a diffuse reflector are shown in (a), (b), and (c). In (d), the total probability of the arrival time over all possible interaction depths in the crystal is shown, where the probability of interaction and time of flight of annihilation photons before interaction are taken into consideration.

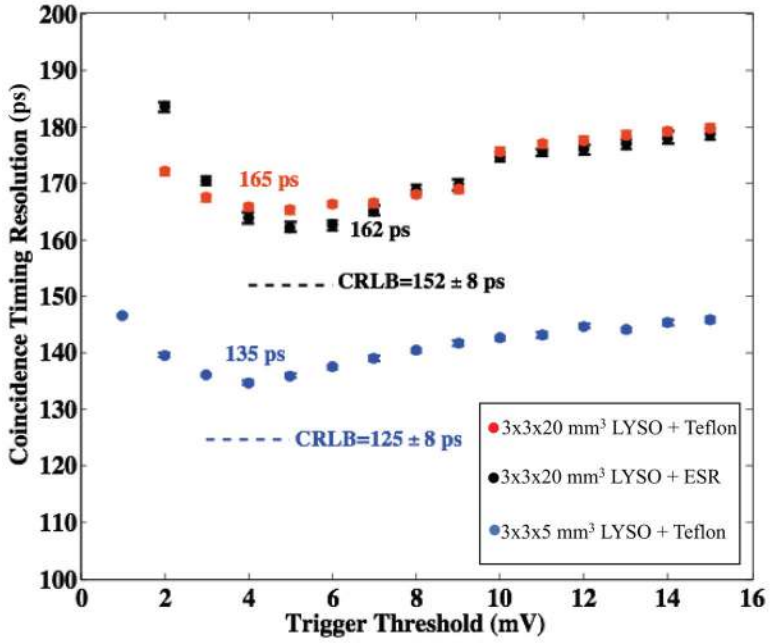

Figure 8.

The measured CTRs for 3×3×5 mm^3 and 3×3×20 mm^3 LYSO:Ce crystals at the optimum LED threshold and SiPM bias V_{br}+4.6 V are shown versus the calculated lower bound on timing resolution for these experimental setups.

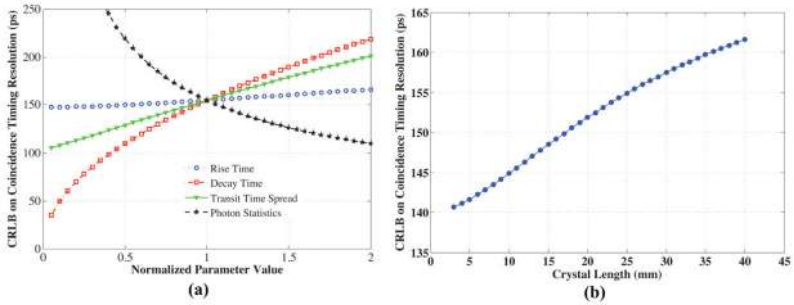

Figure 9.

The calculated *CRLB* on the CTR for the experimental setup described in Section II. D is shown as different parameters in the calculation are varied.

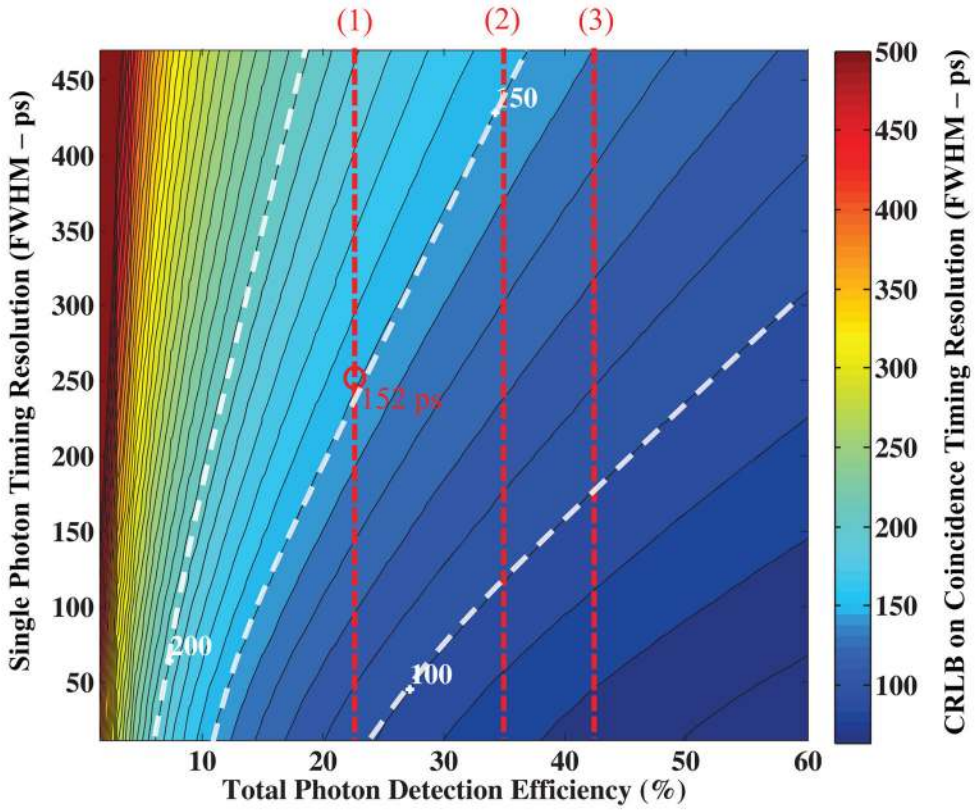

Figure 10.

The *CRLB* on the CRT between two identical 3×3×20 mm^3 LYSO:Ce detectors is shown as total detection efficiency (light collection and PDE) and single photon timing resolution were parametrically varied.